Characterization of the corrosion layer on iron archaeological artefacts from K2 (825-1220 AD), an archaeological site in South Africa

Farahnaz Koleini[1], Linda C. Prinsloo[2], M.H. Schoeman[3], Innocent Pikirayi[1], Shadreck Chirikure[4]

Abstract:

A study of the composition and phase distribution of the corrosion layers on three ferrous objects, excavated at K2 (Bambandyanalo), an archaeological site in South Africa, was conducted. The objective of the study was to obtain information that can contribute to conservation procedures to be performed on the iron artefacts from this site. Examination of cross sections by means of SEM-EDS, XRD and micro-Raman spectroscopy revealed the same corrosion composition and structure for all the objects under study, namely an internal layer adjacent to the metal surface with ghost inclusions and an external layer containing quartz grains. The study also revealed that the presence of magnetite (Fe_3O_4), maghemite (γFe_2O_3) and lepidocrocite (γ-FeOOH) within the internal layer is the only difference between the chemical compositions of iron corrosion products within the two layers. The results also made it possible to retrace the corrosion history during burial and long term storage.

Keywords: *Archaeology; Iron artefacts; Conservation; Corrosion; Micro- Raman; Bambandyanalo*

Introduction

K2 or Bambandyanalo archaeological site was an Iron Age settlement (825-1220 AD) located in the middle Limpopo river valley in South Africa (Fig.1), close to the confluence of the Limpopo and Shashe rivers which form the borders between South Africa, Botswana and Zimbabwe (Meyer, 1998; Vogel, 1998; Huffman, 2005, 2007). The historical metallurgy of the Shashe-Limpopo region, a part of sub-aharan Africa, is different than that of

[1] Department of Anthropology and Archaeology, University of Pretoria
[2] Department of Physics, University of Pretoria
[3] Department of Archaeology, University of the Witwatersrand
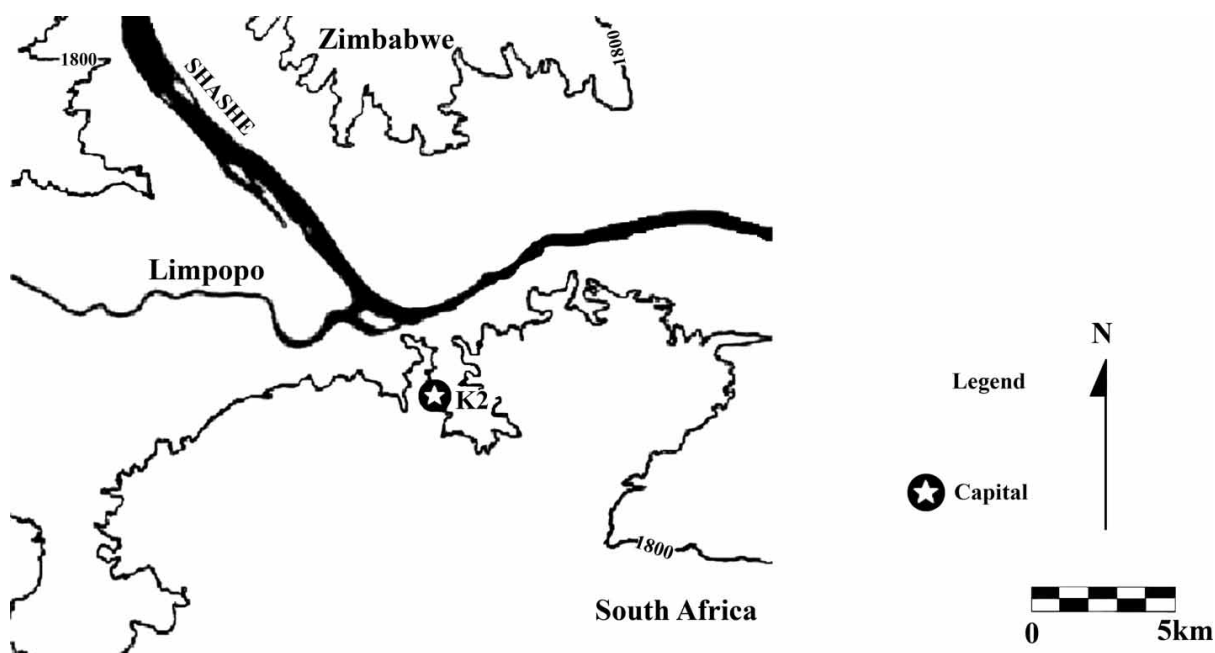[4] Department of Archaeology, University of Cape Town

Figure 1. The location of K2 site in the middle Limpopo valley. Adapted from: Huffman (2000)

Mediterranean North Africa, the Nile Valley, and the Red Sea coast regarding its chronology, technology and mechanism of indigenous metal production (van der Merwe, 1980; Miller & van der Merwe, 1994). While the advent of metallurgy in the Nile Valley occurred about 5000 - 4000 BC with the use of copper (Tylecote, 1976; Miller & van der Merwe, 1994), in sub-Saharan metallurgy the appearance of copper and iron seems to have been simultaneous and there is no sign of prior copper metallurgy or a former Bronze Age period in this region (Tylecote 1976; van der Merwe, 1980; Miller & van der Merwe, 1994). Metal technology was probably introduced to southern Africa in the first millennium AD and by 500 AD the production of iron was widespread (Friede & Steel, 1975; van der Merwe, 1980; Denbow, 1990; Miller & van der Merwe, 1994).

K2 was the capital of the Leopard's Kopje cluster and their subsistence depended on farming and herding as well as trading with nearby consumers and overseas merchants (Axelson, 1973; Voigt, 1983; Huffman, 2000; Miller, et al., 2000). Numerous ferrous artefacts were unearthed at K2 during archaeological excavations in the past decades (1930-1990) (Meyer, 1998). The artefacts are kept in different states of preservation at the Mapungubwe Museum at the University of Pretoria. In order to obtain information regarding the chemical stability of the objects, three representative artefacts from this assemblage, ranging from low to heavily corroded ones were selected to characterize their corrosion

2

structure as well as to determine chemical composition of the corrosion products. These objects were excavated between 1936 and 1972.

Investigations on iron corrosion are significant not only for applications in industry, but also for the conservation of archaeological artefacts and a number of papers have been written concerning various aspects of corrosion such as the mechanism of corrosion formation (Nicholls, 1973; Krauskopf, 1979; Turgoose, 1982; Blesa *et al*., 1994; Selwyn *et al.* 1999), phase characterization (Neff *et al*., 2005), arrangement (Bertholon, 2000; Neff *et al*., 2005) and stability (Misawa, 1973; Krauskopf, 1979). The results of these studies show that the chemical and physical characteristics of the environment have a direct and complicated effect on corrosion composition and structure. However, a variety of corrosion products were detected in different environments; the main phases in both aerobic soil and in an atmospheric environment generally consist of a range of iron oxides and oxyhydroxides. In corrosion studies, detecting the exact phase composition usually presents some difficulties, which mostly originate from complexities within the chemical composition of each phase. In this regard, different analytical techniques are usually utilized in conjunction to identify the accurate composition of different phases. In this study we used X-ray powder diffraction (XRD), energy-dispersive spectroscopy coupled to scanning electron microscope (SEM-EDS) and micro- Raman spectroscopy as complementary methods to identify corrosion products. The latter two methods made it possible to characterize different phases of corrosion directly on the samples on a microscopic scale. The analytical results led us to estimate the chemical stability of the objects and revealed the limit of the original surface within a variety of corrosion products, which is important data for later treatment procedures. In this paper, we first present the microscopic data on the corrosion structure on the objects followed by the analysis and results of corrosion composition and phase distribution on the surface. On the basis of the results we also endeavoured to retrace the corrosion history of the objects during interment and later storage in atmospheric conditions.
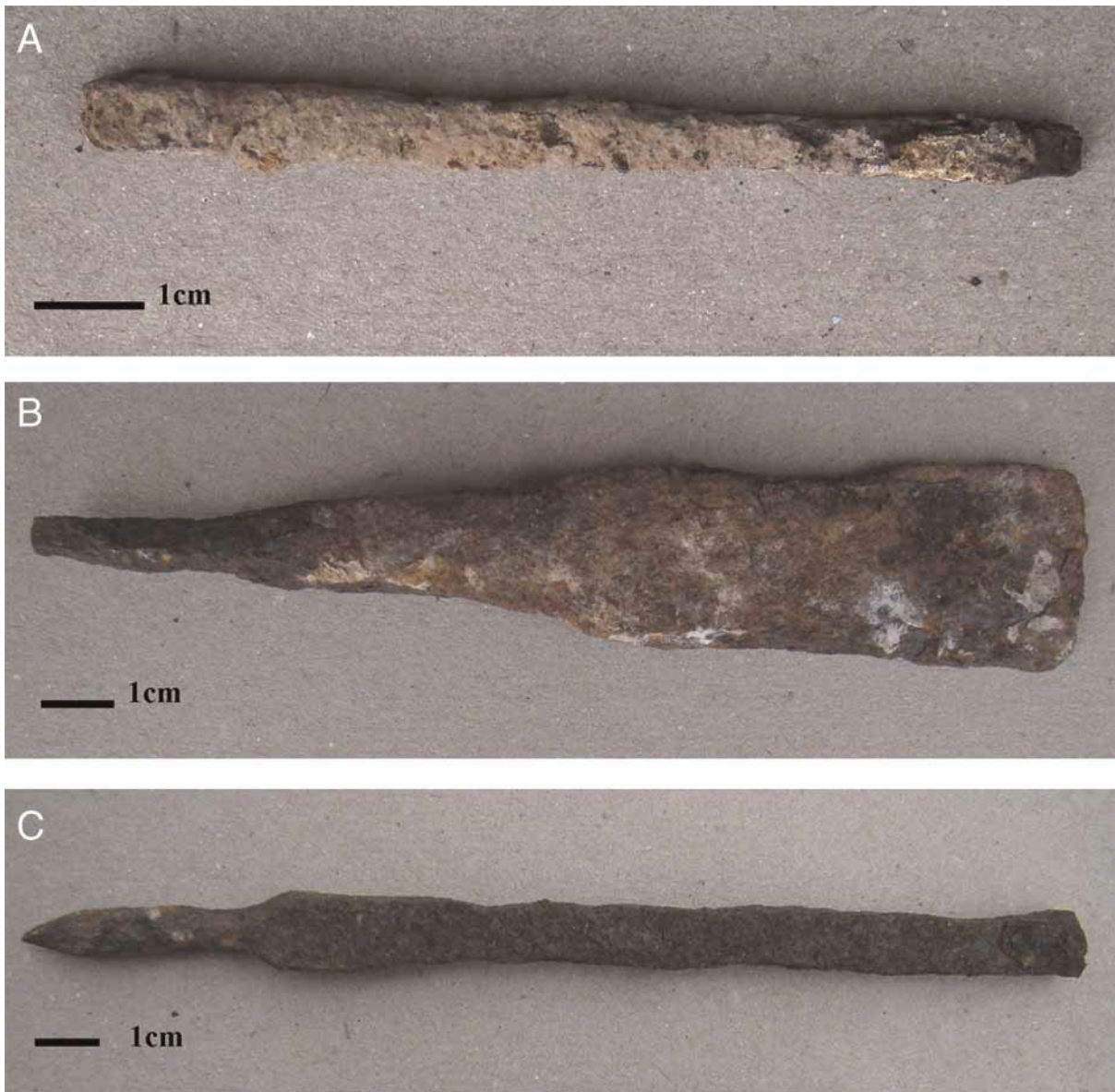
Figure 2. Three iron objects from K2; a) KI1, Bar b) KI3, Adze c) KI5, Drill

Sample characteristics and environmental context

The artefacts examined in this study are three iron objects excavated at K2 (Fig. 2) with different corrosion percentages and dimensions (Table 1). Metallography of the samples shows the objects were fabricated from inhomogeneous hypoeutectoid steel with ≤0.2% carbon by weight. The carbon content of the metal phase (iron-carbon alloy) was estimated in a qualitative way by comparing the volume fraction of pearlitic zones in micrographs of the samples to reference data with the same magnification published in Samuels (1980). A small

Table 1 Characteristics of the objects

Objects	Weight (g)	Length (mm)	Corrosion (%)	Fabrication
Bar (KI1)	11.5	87.39	53	Annealed
Adze (KI3)	104.1	137.25	37	Normalized
Drill (KI5)	43.4	162	15	Normalized

amount of silicon (0.1-0.2%) within the bulk of metal, which is probably due to finely dispersed silicate inclusions, was the only other impurity detected in KI1 and KI3 by SEM-EDS (Table 2: analysis KI1; KI3).The metal phase in KI5 also contains 0.7wt% nickel in addition to silicon (Table 2: analysis KI5). A small percentage of Ni, not exceeding 1%, indicates this is rather a smelting product than an intentionally alloy. Ni originated from an iron ore that had different composition in comparison with the ores that were utilized to fabricate the other two objects. The metallic core in the objects also contains numerous heterogeneously dispersed inclusions with different compositions (Table 2).The corrosion percentage of the artefacts was determined using neutron tomography results and utilizing of IMAGJ open source software which was discussed thoroughly elsewhere (Koleini, et al., in press). The objects are stored at 65% Relative Humidity (RH) with almost ± 10% seasonal fluctuation in storage. Before excavation the objects were buried in well-aerated homogeneous silty sand with a low alkalinity (pH 8-9). Soil samples taken from different depths at the site during past excavations revealed the presence of chlorine, varying in concentration between a minimum concentration of 511 mg/kg close to the surface (30 cm) and a maximum of 964.3 mg/kg at a depth of 90 cm (Koleini, in preparation).

Table 2 Elemental composition of metallic core and inclusions (EDX results/wt%)

Object	Target	O	Na	Mg	Al	Si	P	K	Ca	Ti	Mn	V	Fe	Ni	Mo
KI1	Metal					0.1							99.9		
KI1a*	Slag	38.5	0.3	0.6	3.5	12.8	0.4	0.6	2.7	0.1	0.6		39.4		0.2
KI1a1	Wüstite	30.7				0.1							69.2		
KI3	Metal					0.2							99.8		
KI3a	Slag	44.3			4.1	18	0.5	0.9	4.4	0.7		0.3	26.6		0.2
KI3b	Glass	53.5	0.9	0.5	3.4	27.8		1.5	3.2	0.4			8.6		0.2
KI5	Metal					0.1							99.2	0.7	
KI5a	Fayalite	31.4	0.2	1.3	0.3	13.6	0.1		1.4		1.9		49.7		
KI5a1	Wüstite	21.9		0.1	0.2	0.3					0.8		76.5		
KI5b	Slag	40.8	0.5	1	1	13.4	0.3	1	2.3		2.3		37.4		

Note: *Letters are indicators of different inclusions.

Analytical procedure

In order to study the corrosion structure and composition of the samples, a small piece ($3mm^3$) of each object was cut off and mounted in resin. The samples were ground with silicon carbide paper up to grade 1200 and then polished with diamond paste down to grade 1 micron with an ethanol base lubricant, to prevent any chemical alteration in the corrosion composition. For XRD analysis, small amounts of corrosion products were scraped off from different parts of the surface (KI1) by using a scalpel. The high porosity of corrosion products aided the easy removal of the sample without inducing any extra pressure to cause friction between the object surface and the scalpel blade. This helped to reduce the risk of contamination within the sample caused by contact with the scalpel blade.

For quantitative elemental identification of corrosion products and a detailed study on phase distribution in the corrosion crust a Jeol 5800 SEM coupled with a Thermo scientific Energy Dispersive X-ray micro-analysis system (SEM-EDS) with a Nano Trace Si(Li) detector was utilized. The analyses were performed under an accelerating voltage of 20 kV and mostly in raster mode on well polished mounted samples which were coated with a thin layer of carbon to prevent electrical charge. In this mode the area analysed varied and depended on the size of phases. The live time was 100s to improved background to peak signal.

To elucidate the exact crystalline structure of the corrosion products, XRD analysis was performed qualitatively using a PANalytical X'Pert Pro powder diffractometer with X'Celerator detector. The sample was scanned at the required 2θ angle ranges from 5 to 90° with step size 0.0084°. The radiation was Fe-filtered CoKα radiation in order to eliminate fluorescence which would cause, high background and poor peak to background ratio. The phases were identified using X'Pert Highscore plus software. For routine phase identification a particle size of less than 50 μm is required, which was achieved by hand grinding in an agate mortar, and then top loaded onto a zero-background holder due to small sample size.

Micro-Raman spectrometry was performed using a T64000 spectrometer from HORIBA Scientific, Jobin Yvon Technology (Villeneuve d'Ascq, France). The Raman spectra were excited with the 647.1 nm line of a Krypton Argon mixed gas laser (Coherent, Innova 70c) with laser power less than 1mW on the surface of the samples. A 50x objective on an Olympus microscope was used to focus the laser beam (spot size ~ 12 μm) on the samples

and also collected the backscattered Raman signal. An integrated triple spectrometer was used in the double subtractive mode to reject Rayleigh scattering and dispersed the light onto a liquid nitrogen cooled Symphony CCD detector. The spectrometer was calibrated with the silicon phonon mode at 520 cm^{-1} before performing the analysis.

Results and discussion

Corrosion stratification

A study of the transverse sections of the objects with SEM revealed a bi-layer corrosion on the surface without consideration of corrosion percentage and the size. This structure is obviously similar to what was proposed with regards to ferrous artefacts corroded in soil by Neff et al. (2005) and consists of two main layers:
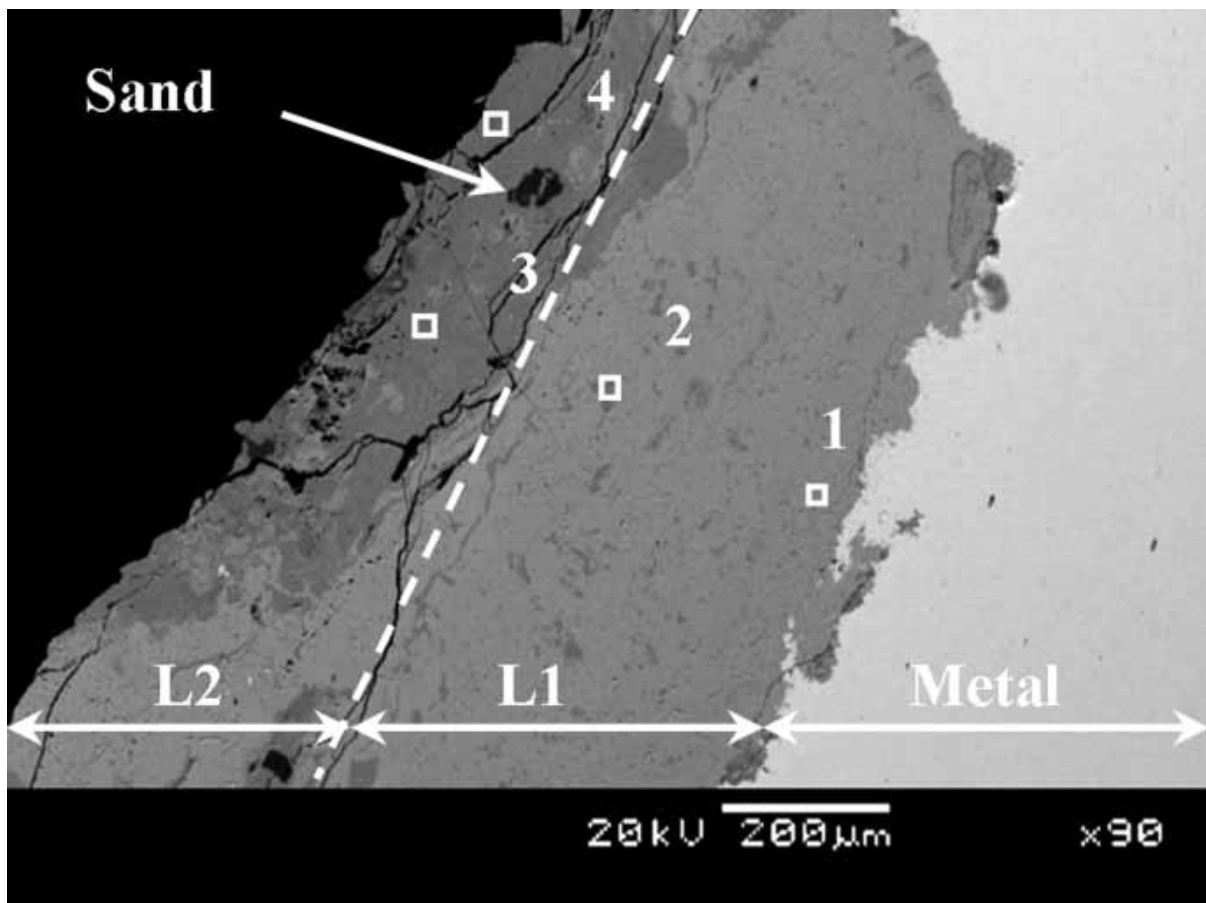

Figure 3. Microstructure of corrosion layers on KI1 (SEM BEI) and positions of electron probe analyser within corrosion layers. The dashed line shows the limit of the original surface.
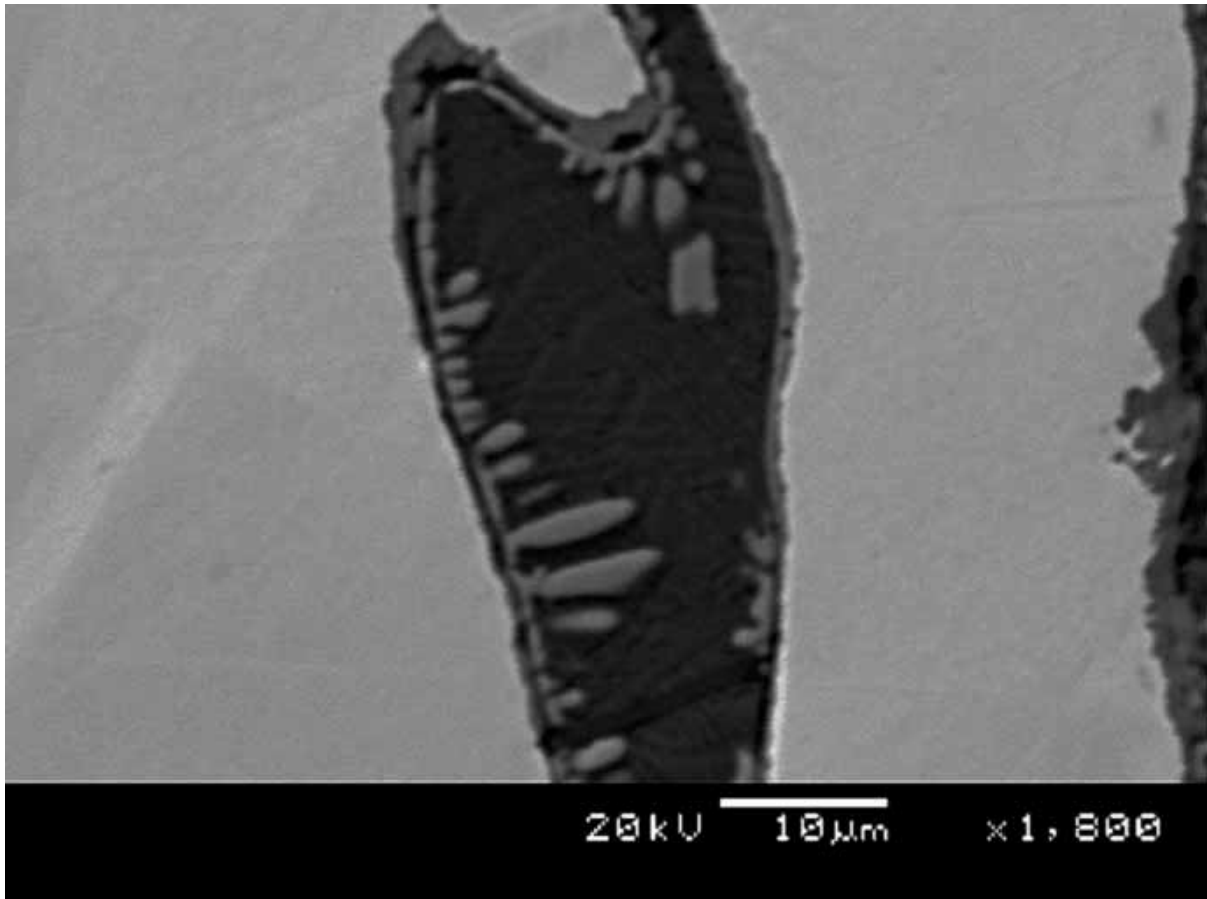
7

Figure 4. Polished section of KI1 at metal substrate (SEM BEI) showing bloomery two-phase inclusion of wüstite dendrites in dark slag with Mo content (0.2%).

1. An internal layer (L1) adjacent to the metal surface consisting of different phases of iron compounds which can be seen as different contrasts in a complex structure (Fig.3). The ghost form of two phases of bloomery inclusions which have been dispersed within the metal core are observable in this layer (Figs.4 and 5). This indicates that this layer was part of the object which had been completely corroded. At the corrosion/metal interface in some areas corrosion penetrated to the metal core along these inclusions.

An external layer (L2) consisting of grains of silica (SiO_2) imbedded in various compounds of iron. The source of silica is the soil in which the object was buried.
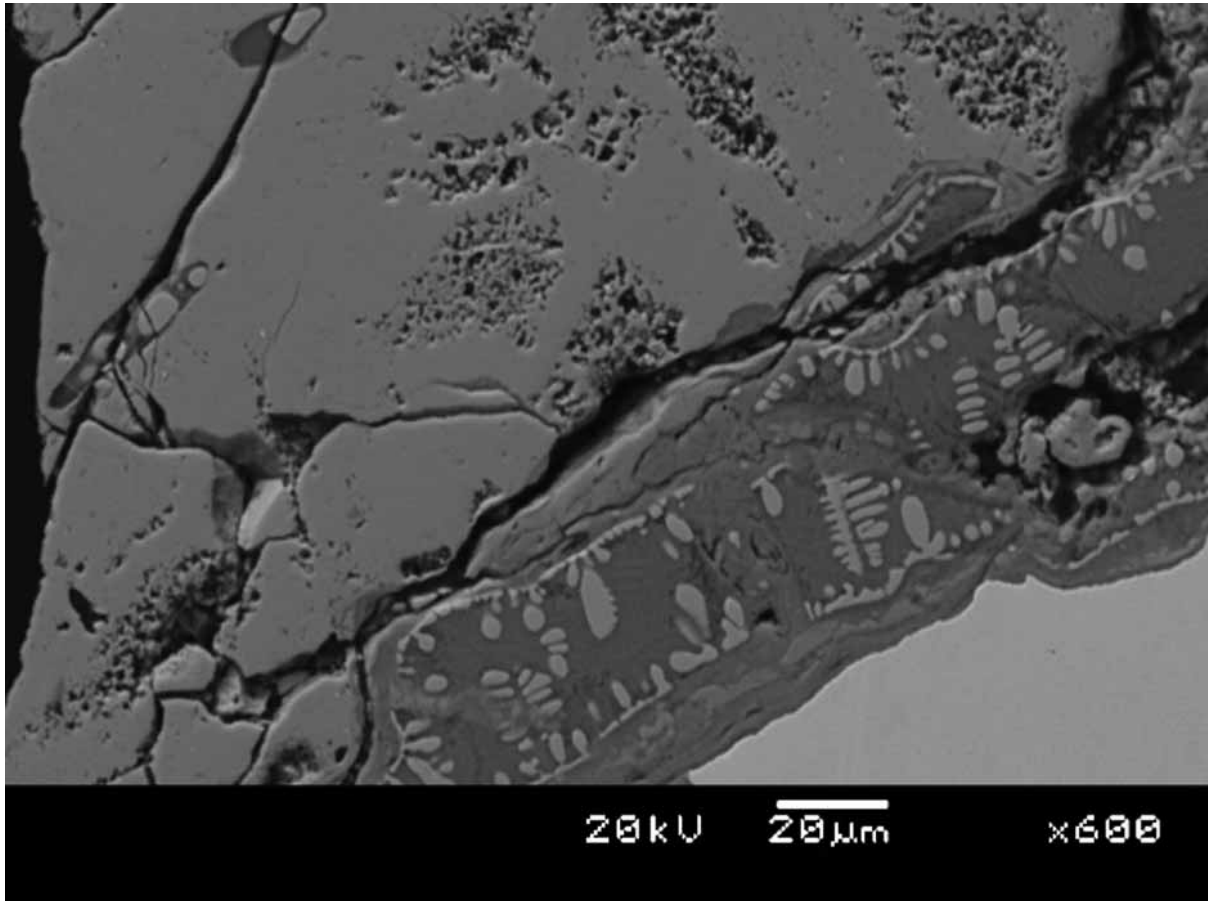
Figure 5. Microstructure of corrosion layers on KI1 (SEM BEI). Remnant bloomery inclusion at internal layer.

Both layers are porous in their structure and contain numerous tiny cracks. The wide, open crevices in these layers were formed during sampling and are quite new (Figs.3 and 5) while the cracks that were filled partially by corrosion products were formed during the growth of the corrosion layer (Fig.6). EDS results revealed internal and external layers containing different phases of iron products such as iron oxides or oxy-hydroxides with different proportions of oxygen within their chemical structure (Table 3). The phases have non-distinctive stratification and irregular dissemination in the internal and external layers. These characteristics show the silica grains and remnant inclusions are the only overt indicators of the barrier between the limits of the original surface and fossilized burial environment (soil) on the surface (see discussion by Bertholon, 2000).
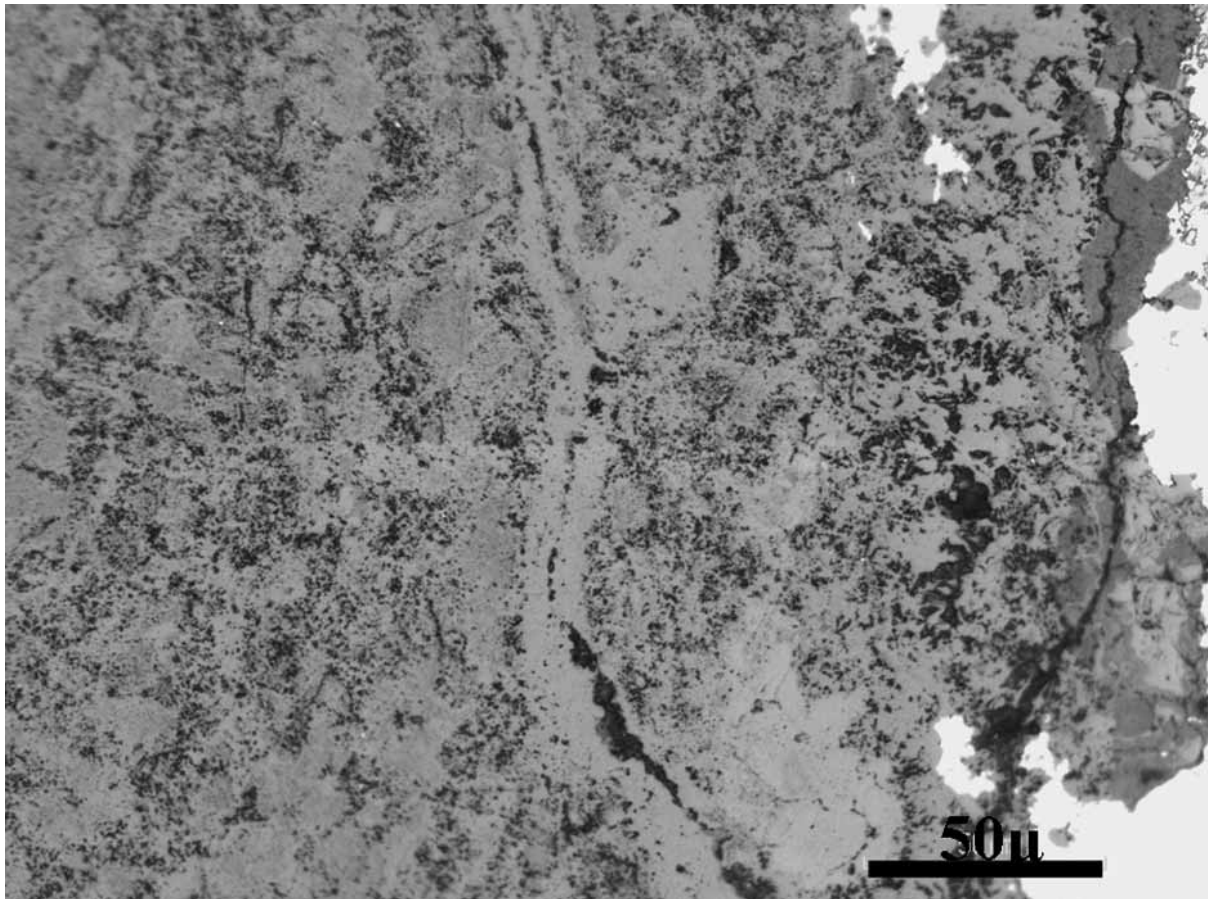
Figure 6. Optical microscopic image of internal layer shows fine cracks together with a porous dark phase.

Table 3 Elemental composition of corrosion phases on iron artefacts (EDX results/wt%)

Objects/ layer	O	Na	Mg	Al	Si	P	Cl	Ca	Fe	Mo
KI1(L1)1	32.9								66.9	0.2
KI1(L1)2	41.5	0.2			0.2				58.1	
KI1(L2)3	43.3		0.1		0.7	0.1		0.2	55.6	
KI1(L2)4	46.2		0.2		3.3	0.7		1.1	48.5	
KI3(L1)a	37.6				0.1				62.2	
KI3(L1)b	47.7				0.1	0.1			52	
KI3(L2)a	38.2		0.1		1.2			0.2	60.2	
KI3(L2)b	47.5		0.1		0.4	0.1		0.2	51.7	
KI5(L1)a	27.8				0.1	0.1			71.9	
KI5(L1)b	35.5				0.1				64.4	
KI5(L2)a	46.8		0.1	0.1	1	0.1			51.9	
KI5(L2)b	37.1		0.2	0.1	1.3	0.1	0.1	0.1	61	

Note: * L1, internal layer; L2, external layer; small letters are indicators of different positions of electron probe within the corrosion layers.

Corrosion composition

Compositional examinations of existent corrosion compounds on the surface of artefacts show similarity in their chemical structure. EDS compositional analyses on positions one, two, three and four in Fig. 3 show that iron and oxygen are the main elemental constituent of corrosion products. Meanwhile, the light grey phase has lower amounts of oxygen (Table 3: analysis KI1(L1)1) in comparison to the darker phases of the internal and external layers (Table 3: analysis KI1 (L1)2; (L2)3, 4). Analysis of the internal layer in positions one and two (Table 3: Analysis KI1(L1)1,2) shows low amounts (0.2%) of Mo, Na and Si that might originate from remnant fine inclusions or simply were transported inwards from the environment. Since Na and Mo were not detected within the external layer (Table 3: Analysis KI1(L2)3,4) it is most likely they were derived from the entrapped slags with Mo and Na content present in the metal matrix (Table 2. analysis KI1a). In general the source of Mo and Na in addition to the other elemental constituent of inclusions within the metallic core can be the ore, furnace wall or even fuel. The extraneous elements in the external layer have more diversity (Si, Ca, Mg and P) while their amount increases towards the surface (Table 3. Analysis (L2) in KI1, KI3, KI5). Corrosion phases within two distinct layers on the surface of KI5 have no Ni content (Table 3. analysis KI5(L1)a,b; (L2)a,b). There was also no trace of chlorine detected by EDS in corrosion layers (Table 3).
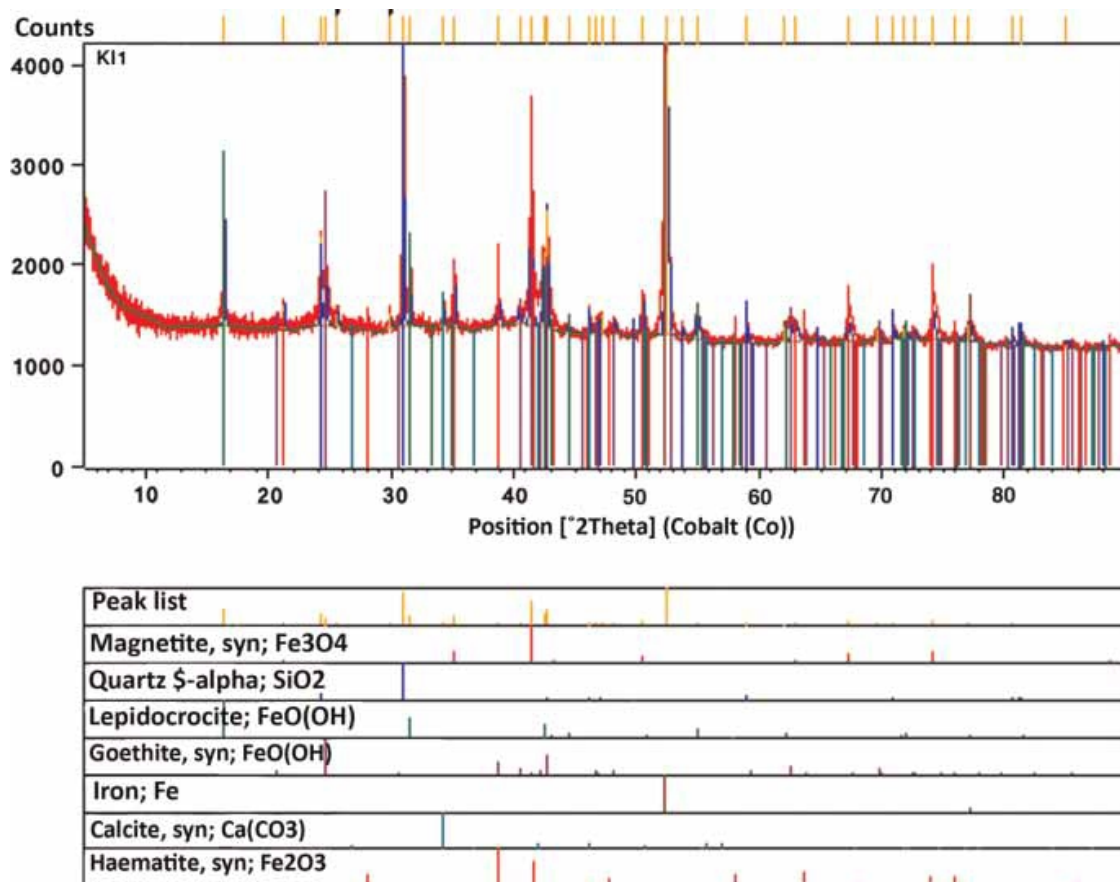

Figure 7. XRD scan of corrosion powder removed from KI1 surface.

Complementary analysis of corrosion products on KI1 was performed with XRD to identify the exact composition of products on the surface. The results revealed the presence of magnetite (Fe_3O_4), lepidocrocite (γ-FeOOH), goethite (α-FeOOH), hematite (Fe_2O_3) and calcite as the main compounds in the crystalline form within corrosion layers (Fig.7). On the basis of EDS results the detected calcium carbonate is related to the surface contaminations concentrated in the external layer (Table 3: analysis KI1(L2)3,4).
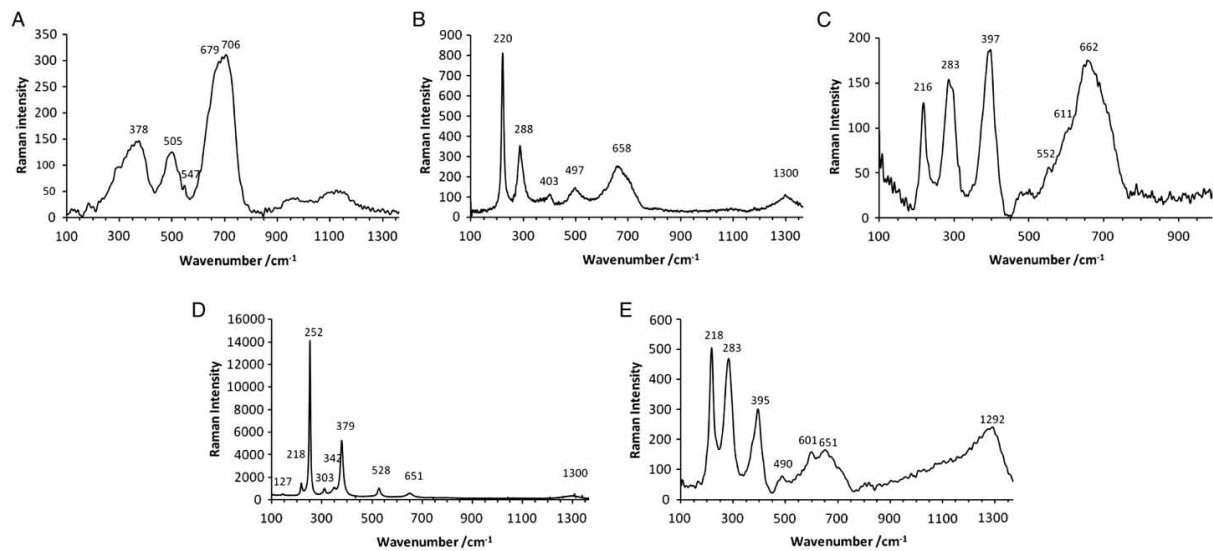

Figure 8. Raman spectra of corrosion products on KI1. λ_0= 647.1 nm. (A) Light phase at internal layer (maghemite). (B) Light phase at internal layer (hematite). (C) Dark phase at internal layer shows admixture of magnetite, goethite and hematite. (D) Lepidocrocite at interface of internal/external layers. (E) Dark phase at external layer shows mixture of hematite and goethite.

Further *in situ* analyses of the mounted samples with micro-Raman spectroscopy identified the position of different phases through their Raman spectra. Identifying the exact composition of each phase was achieved by comparing the results with the Raman spectra of iron oxides/hydroxides published in Bell et al. (1997) and Froment et al. (2008). For facilitating the interpretation of the Raman data the spectral signatures of pure iron oxides and hydroxide are summarised in Table 4. The Raman spectra obtained on the light grey areas in the internal layer are presented in Fig. 8A and 8B. Spectrum (a) with a broad and

Table 4 Raman peaks of pure iron oxides and hydroxides

Magnetite Fe$_3$O$_4$	Maghemite γFe$_2$O$_3$	Haematite αFe$_2$O$_3$	Haematite* Fe$_2$O$_3$ (synthetic)	Goethite αFeOOH	Lepidocrocite γFeOOH
				205 (w)	
		225 (vs)	224 (vs)		
		240		245 (w)	250 (vs)
310 (w)		290 (vs)	291 (vs)	300 (m)	300 (w)
	380 (m)			390 (vs)	380 (m)
		405 (m)	407 (m)	415	
	460 (m)	495 (w)	494 (w)	480 (w)	
540 (m)	510 (m)			550 (w)	525 (w)
		605 (m)	610		650 (m)
670 (vs)	670 (s)		660 (w, sh)	685 (m)	
	720 (vs)				

Note: w, weak; s, strong; vs, very strong; m, medium; sh, shoulder; the data adapted from * Bell *et al.*, (1997) and Froment *et al.*, (2008).

strong peak at 679-706 cm^{-1} and weak peaks at 378 and 505 cm^{-1} belong to maghemite (γFe$_2$O$_3$). The weak peak at 547 cm^{-1} may relate to magnetite (Fe$_3$O$_4$) as a part of a material constituent of this phase. The strong peak of magnetite at 670 cm^{-1} overlaps with the broad peak of maghemite in this region. Spectrum (b) is typical of hematite (αFe$_2$O$_3$) with strong double peaks at 220 and 288 cm^{-1}, weak peaks at 403 and 497 cm^{-1} as well as a medium peak at 658 cm^{-1}. The Raman spectrum (c) in Fig. 8 corresponds to the dark grey phase at the internal layer and consists of various bands that can be attributed to an admixture of magnetite, goethite and hematite. Signature doublet strong peaks of hematite with a downshift are observable at 216 and 283 cm^{-1} while the latter is quite broad as a result of overlapping with a goethite medium peak at 300 cm^{-1}. It has been shown that the Raman spectrum of hematite is very dependent on particle size and morphology, production process, orientation of the crystallites, as well as the energy of the exciting radiation (Chernyshova *et al.,* 2007). The shift to lower wavenumbers might be any of these. The strong peak at 397cm^{-1} is characteristic of goethite and overlaps with the weak hematite peak at 403cm^{-1} (Fig.8B) with resultant peak broadening. The shoulder at 482-519 cm^{-1} is due to the overlapping of the goethite and hematite weak peaks at 480 and 497 cm^{-1} respectively. The weak peak at 552 cm^{-1} is associated with goethite whereas the medium peak at 611 cm^{-1} belongs to hematite. The strong broad peak at 662 cm^{-1} can be the signature of magnetite for which in a pure sample is observed at 670 cm^{-1}. Peak broadening is due to the overlapping of the goethite and hematite peaks in this region. A strong peak at 661 cm^{-1} was also reported for a freshly fractured magnetite crystal face at room temperature in de Faria et al. (1997). Figure 8D shows the Raman analysis of a well crystallized area at the interface of the internal/external layer. The strong peak at 252 cm^{-1}, medium peak at 379 cm^{-1} in addition to the weak peaks at

303, 528 and 651 cm^{-1} are the Raman characteristics of lepidocrocite (γFeOOH). The Raman spectrum (e) in Fig. 8 is related to the dark phase in the external layer and shows that it mostly consists of hematite and goethite. In Fig. 8E the doublet strong peaks at 218 and 283 cm^{-1} are the signature of hematite whereas the strong peak at 395 cm^{-1} is characteristic of goethite. Analysing on light phases at external layer rising to a spectra similar to Fig. 8B and revealed that this phase mostly contains hematite.

Taking all the analytical results into consideration, the distribution of different corrosion compounds on the surface of the objects is as follows:

1. At the internal layer, corrosion has an inhomogeneous composition mostly of different oxides and hydroxides of iron such as magnetite, hematite, maghemite, goethite and lepidocrocite. In this layer, phases with mixed compositions of magnetite, goethite and hematite are detected along with homogenous phases of hematite, maghemite and lepidocrocite.

2. At the external layer the homogenous phase of hematite is mostly observed next to the inhomogeneous phases mostly containing a mixture of hematite and goethite.

Retracing corrosion formation

Taking into consideration that a long time has passed since the objects were excavated, the detected corrosion products on the surface are predominantly the stable chemical forms of the unstable ones that appeared during the incipient stages of corrosion during burial. Nevertheless the identified products are quite informative for retracing the history of burial and later storage. Electrochemical corrosion of archaeological iron before and after excavation was discussed thoroughly by Turgoose (1982, 1985) and Selwyn *et al.* (1999). In this process, ferrous ions produced via oxidizing of iron in anodic zones react with cathodic products (OH$^-$ and H$_2$O) that are formed by means of oxygen reduction. In view of the fact that the burial environment at K2 had sufficient chloride content to participate in corrosion process, lack of chlorides with their high mobility (Turgoose, 1982) at anodic zones at the metal/corrosion interface indicates that the cathode was on the metal surface during burial. In general isolation of anodic zones from cathodic areas results in increasing the concentration of anions mostly chloride, near the metal surface during burial (Turgoose, 1982) which was not the case here. Since the burial environment at K2 was well-aerated silty sand (Meyer, 1998; Koleini, in preparation), oxidation of the metal surface was the first stage in
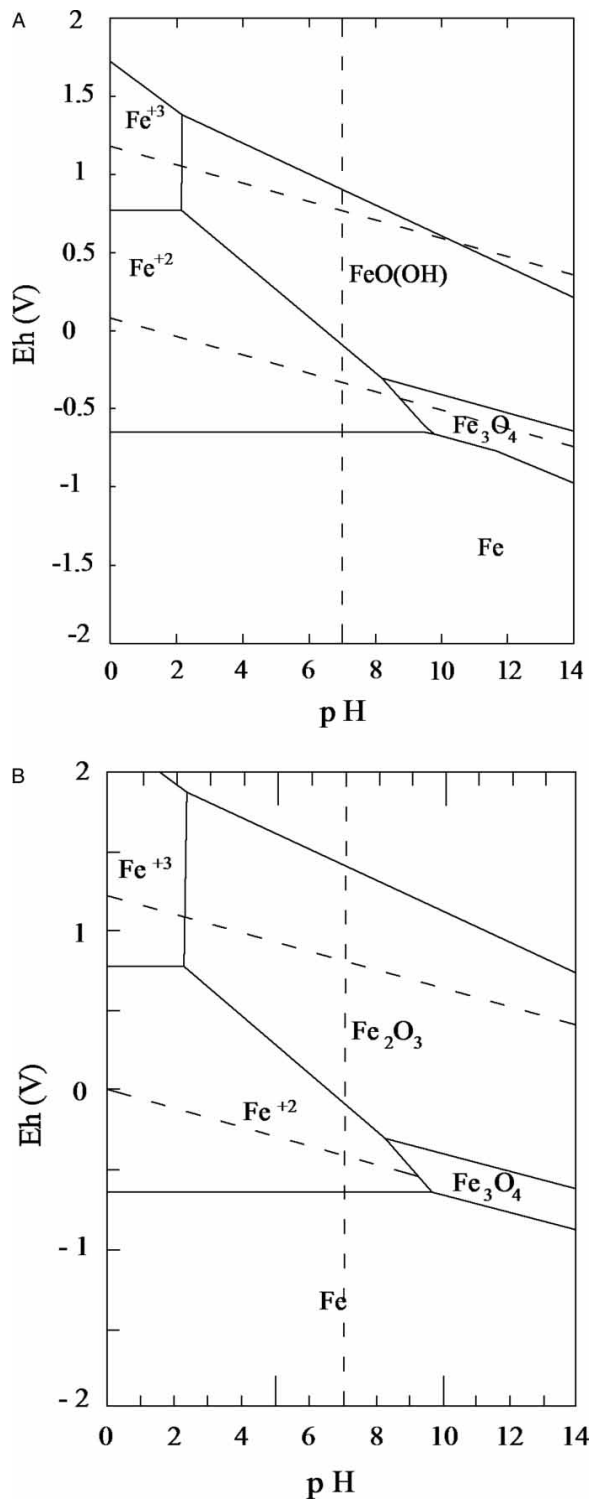
Figure 9. Eh-pH diagrams for the system Fe-H₂O at 25°C. (A) Range of stability of iron(III)oxyhydroxide and magnetite along with stability domain of ferrous ions. (B) Range of stability of hematite. Adapted from: Beverskog and Puigdomenech (1996).

electrochemical corrosion of the iron objects. This process resulted in formation of Fe^{2+} ions at the metal surface which reacted with cathodic products to produce iron(II)hydroxide. With

consideration of a high amount of dissolved oxygen in the water content of the soil, as well as soil alkalinity (pH>6), the unstable iron(II)hydroxide was rapidly oxidized to iron(III)hydroxide (Nicholls, 1973; Blesa *et al*., 1994). With time iron(III)hydroxide was converted to iron(III) oxyhydroxides (FeOOH) (Misawa ,1973), which were detected at regions with high oxygen access at internal and external layer. In this time, the rate of corrosion as well as dissolution of metal into the environment was high; the sand particles were entrapped among the corrosion products. Precipitation of porous insoluble products along with soil particles on the surface resulted in passivation of the metal surface while the penetration of dissolved oxygen was only possible along the small cracks and pores which were formed during growth of the corrosion layer by volume expansion of corrosion products on the surface (Fig.6). In this stage Fe^{2+} ions, on the basis of their domain stability (Fig.9), were diffused in pores and cracks that were saturated with water and precipitated as magnetite in areas with limited oxygen access in the form of inter-dispersed phases in iron(III)oxyhidroxides at internal layer (dark phase). In places with higher oxygen access, the Fe^{2+} ions were converted to iron(III)oxyhydroxides such as goethite and lepidocrocite at internal and external layer.

In fact, the diffusion domain of Fe^{2+} ions across corrosion crust toward surface was completely controlled by Eh and pH of corrosion layers' microenvironment. This domain depends on the range of stability of the ferrous ions in specific quantity of Eh and pH that were considered in Pourbaix diagram (Fig.9). With ageing of the corrosion crust, the unstable products gradually transformed to more thermodynamically stable ones. In this process lepidocrocite that usually forms first in transformation of Fe(III)hydroxide was converted to goethite (Stratmann, 1990) while goethite (α-FeOOH) partly altered to hematite in some areas (light phase). The free energy formation of the later reaction is small and enables goethite to remain for a long time (Krauskopf, 1979; Turgoose, 1982) along with more stable products such as hematite. Metastability of lepidocrocite, in addition to its formation which is associated with a high quantity of Fe^{2+} ions in area of formation (Cornell & Schwertmann, 2003), creates this possibility that the corrosion is still continuing in atmospheric condition. Maghemite, which was detected along with magnetite in the internal layer (Fig.8A) could be formed by oxidation of magnetite (Cornell & Schwertmann, 2003) in areas with higher oxygen access, and probably after excavation. On the other hand, lack of maghemite within the discovered corrosion compounds in XRD analysis can be due to its metastability and easy

transformation to hematite by powdering that was reported in Romdohr (1969). The results also indicate that low amount of Ni in KI5 metal phase as impurity has no effect on type of corrosion products detected on the surface. Takahashi *et al.* (2005) suggested nickel content can affect only the fraction of goethite and magnetite within a major lepidocrocite constituent. In this study paucity of the samples prevented of quantitative analysing of corrosion products.

Conclusion

The study of the corrosion structure on the surface of three representative samples from K2 by means of SEM-EDS, XRD and micro-Raman revealed the same corrosion stratification on their surface. The corrosion crust that was formed in a well aerated burial environment, and later by continuing corrosion in atmospheric conditions during storage, consists of an internal and external layer with inhomogeneous composition. Iron(III)oxyhydroxides (goethite and lepidocrocite) along with iron oxides such as magnetite, maghemite and hematite were detected on the surface whereas magnetite , maghemite and lepidocrocite were restricted to the internal layer. Composition of products on the surface of these artefacts, which consists of iron(III) oxyhydroxides and iron oxides, revealed corrosion formation was under the effect of diffusion of dissolved oxygen in water through pores and cracks toward metal surface. Lack of anions such as chloride originating from the surrounding soil at the metal/corrosion interface indicated the cathodic zones were placed on the metal surface during burial. The presence of unstable lepidocrocite in the internal layer can be a sign for continuity of corrosion in atmospheric conditions of damp storage. The study also revealed the capabilities of micro-Raman in identifying a combination of different iron corrosion products together.

References

1. Axelson, E. 1973. *South-East Africa 1488-1600*. Johannesburg: Struik LTD.

2. Bell, I. M., Clark, R. J., & Gibbs, P. J. 1997. Raman spectroscopy library of natural and synthetic pigments (pre- 1850 AD). *Spectrochimica Acta Part A,* 53: 2159-2179.

3. Bertholon, R. 2000. La limite de la surface d'origine des objets métalliques archéologiques, Caractérisation, localisation et approche des mécanismes de conservation. PhD thesis, Université Paris 1 –Sorbonne.

4. Beverskog, B., & Puigdomenech, I. 1996. Revised Pourbaix diagrams for iron at 25-300 ˚C. *Corrosion Science*, 38 (12): 2121-2135.

5. Blesa, M.A., Morando, P.J. & Regazzoni, A.E. 1994. *Chemical Dissolution of Metal Oxides*. London: CRC Press.

6. Chernyshova, I. V., Hochella Jr, M. F., & Madden, A. S. 2007. Size-dependent structural transformations of hematite nanoparticles. 1. Phase transition. *Physical Chemistry Chemical Physics*, 7: 1736-1750.

7. Cornell, R. M. & Schwertmann, U. 2003. *The iron oxides: structure, properties, reactions, occurrences and uses*. Weinheim: John Wiley-VCH.

8. de Faria, D. L. A., Venancio Silva, S., & de Oliveira, M. T. 1997. Raman microspectroscopy of some iron oxides and oxyhydroxides. *Journal of Raman Spectroscopy,*28:873-878.

9. Denbow, J. R. 1990. Congo to Kalahari: data and hypotheses about the political economy of the western stream of the Early Iron Age. *African Archaeological Review*, 8: 139-176.

10. Friede, H. M., & Steel, R. H. 1975. Notes on Iron Age copper-smelting technology in the Transvaal. *Journal of the South African Institute of Mining and Metallurgy*, 75: 221-231.

11. Froment, F., Tournié, A., & Colomban, P. 2008. Raman identification of natural red to yellow pigments: ochre and iron-containing ores. *Journal of Raman Spectroscopy,* 39: 560-568.

12. Huffman, T. N. 2000. Mapungubwe and the origins of the Zimbabwe culture. *Goodwin Series,* 8: 14-29.

13. Huffman, T. N. 2005. *Mapungubwe: Ancient African civilization on the Limpopo*. Johannesburg: Wits University Press.

14. Huffman, T. N. 2007. *Handbook to the Iron Age: The archaeology of pre-colonial farming societies in southern Africa*. Scottsville: University of KwaZulu-Natal Press.

15. Koleini, F. (in preparation). Mapungubwe Metals revisited: A Technical and Historical study of Mapungubwe Material Culture with an Emphasis on Conservation. PhD Thesis, University of Pretoria.

16. Koleini, F., de Beer, F., Schoeman, M.H.A., Pikirayi, I., Chirikure, S., Nothnagel, G., & Radebe, J.M. (in press). Efficiency of neutron tomography in visualizing the

18

internal structure of metal artefacts from Mapungubwe museum collection with the aim of conservation. *Journal of Cultural Heritage,* doi:10.1016/j.culher.2011.11.001.

17. Krauskopf, K.B. 1979. *Introduction to geochemistry,* London: McGraw-Hill.

18. Meyer, A. 1998. *The archaeological sites of Greefswald.* Pretoria: University of Pretoria.

19. Miller, D., & Vander Merwe, N.J. 1994. Early metal working in sub-Saharan Africa: A review of recent research. *Journal of African History*, 35, 1-36.

20. Miller, D., Desai, N., Lee-Throp, J. 2000. Indigenous gold mining in southern Africa: a review. *Goodwin Series,* 8: 91-99.

21. Misawa, T. 1973. The thermodynamic consideration for Fe-H_2O system at 25˚C. *Corrosion Science,* 13: 659-676.

22. Neff, D., Dillmann, P., Bellot- Gurlet, L., & Beranger, G. 2005. Corrosion of iron archaeological artefacts in soil: characterization of the corrosion system. *Corrosion Science,* 47: 515-535.

23. Nicholls, D. 1973. *The Chemistry of Iron, Cobalt and Nickel.* New York: Pergamon Press.

24. Romdohr, P. 1969. *The ore minerals and their intergrowths.* Toronto: Pergamon Press.

25. Samuels, L.E. 1980. *Optical microscopy of carbon steels.* Metals Park, Ohio: American Society of Metals.

26. Selwyn, L. S., Sirois, P. J., & Argyropoulos, V. 1999. The Corrosion of Excavated Archaeological Iron with Details on Weeping and Akaganéite. *Studies in Conservation*, 44:217-232.

27. Stratmann, M. 1990. The atmospheric corrosion of iron—a discussion of the physico-chemical fundamentals of this omnipresent corrosion process; invited review. *Berichte der Bunsengesellschaft für Physikalische Chemie,* 94: 626–639.

28. Takahashi, Y., Matsubara, E., Suzuki, S., Okamoto, Y., Komatsu, T., Konishi, H., Mizuki, J., & Waseda, Y. 2005. In-situ X-ray Diffraction of Corrosion Products Formed on Iron Surfaces. *Materials Transactions*, 46: 637 to 642.

29. Turgoose, S. 1982. The nature of surviving iron objects. In: R.W. Clarke & S.M. Blackshaw, eds. *Conservation of Iron.* Maritime monographs and report 53. England: Yale Press, pp. 1-7.

30. Turgoose, S. 1985. The corrosion of archaeological iron during burial and treatment. *Studies in Conservation,* 30: 13-18.

31. Tylecote, R. F. 1976. *A History of Metallurgy.* London: The Metals Society.

32. van der Merwe. N.J.1980.The advent of iron in Africa. In: T.A. Wertime & J. D. Muhly, eds. *The Coming of the Age of Iron*. New Haven: Yale University Press, pp.463-506.

33. Vogel, J. C. 1998. Radiocarbon dating of the Iron Age sites on Greefswald. In: A. Meyer, eds. *The Archaeological sites of Greefswald stratigraphy and chronology of the sites and history of investigations.* Pretoria: University of Pretoria Press, pp. 296-301.

34. Voigt, E. A.1983. *Mapungubwe: an archaeozoological interpretation of an Iron Age community*. Pretoria: Transvaal Museum.